Article

Multi-Sensor Optimal Motion Planning for Radiological Contamination Surveys by Using Prediction-Difference Maps

Tony H. Shin * [ID]**, Daniel T. Wakeford** [ID] **and Suzanne F. Nowicki**

Space Science and Applications Group, Intelligence and Space Research Division, Los Alamos National Laboratory, Los Alamos, NM 87545, USA; wakeford@lanl.gov (D.T.W.); snowicki@lanl.gov (S.F.N.)

* Correspondence: thshin@lanl.gov

Abstract: Distributed and networked mobile sensor platforms using unmanned aerial and/or ground vehicles to survey areas of interest offer a safer and more efficient method for radiological contamination mapping; however, most applications rely on uniformly sweeping of the area in a raster-type motion without utilizing the information available in a dynamic sense. We have developed a fully autonomous optimal motion planning procedure for networks with two or more mobile sensors. The procedure utilizes well-established concepts of Gaussian processes in combination with control laws based on centroidal Voronoi tessellations to achieve optimal next-iteration sensor movements. A new method of informing optimal motion planning is proposed, whereby the absolute difference between the prior and current full-map prediction, referred to as the prediction-difference map, is used as the spatial density function within each Voronoi cell, providing immediate and iterative feedback for dynamic use of available information. The Gaussian process regression model used to estimate the contamination in unvisited locations also provides prediction uncertainties, and can be used as a quantitative metric to assess the confidence in the calculated contamination map; these estimates and prediction uncertainties are unavailable for standard uniform survey routines as they can only produce maps in the vicinity of observed locations. We present through simulation the achievable performance gains from using this new method by directly comparing to a uniform survey method. Results show that using the prediction-difference maps to inform motion planning procedures offers a faster rate of producing an accurate and convergent map relative to a uniform survey route.

Keywords: radiation mapping; mobile sensors; autonomous

1. Introduction

Distributed and networked unmanned aerial- and/or ground-based vehicles (UAVs and UGVs) for radiological contamination mapping can provide a safer and more efficient option for surveying large areas of interest. The ability to produce a timely and accurate representation of contamination is significant in applications such as nuclear emergency response, tactical mission planning, and post-event procedure development, among others [1–11]. The primary objective for mapping radiological contamination is to make an accurate measurement of the radiation in predefined areas. The aerial/ground coverage by the UAVs/UGVs and the spatial resolution of the measurements are two important aspects that determine the fidelity and efficiency of the mapping technique and motion planning procedure. Adequate coverage of a predefined area ensures that any relatively small contamination features are accounted for in the radiation map. Better spatial resolution of the calculated contamination provides a more detailed and representative map. Both coverage and spatial resolution are dependent on the detector efficiency and prescribed trajectory of the UAV/UGVs. The use of UAVs and UGVs for radiation mapping has been demonstrated in previous works where uniform survey routes are typically employed by using a raster motion trajectory throughout the area [2]. However, these uniform survey routes are unguided by real-time data, making for a less efficient survey, and are only

able to produce maps in the vicinity of where the vehicles have visited previously. Other methods rely on predetermined motion paths and could be considered semi-autonomous, but require a priori knowledge on the nature of the contamination sites. The ability to implement a fully autonomous motion planning procedure that utilizes real-time sensor data would allow for the complete removal of human-in-the-loop dependencies. Table 1 summarizes the advantages and limitations of typical survey methods.

Table 1. Summary of advantages and limitations of typical survey methods for radiological contamination mapping.

Survey Technique	Autonomy	Advantages	Limitations
Uniform survey	Possible through pre-planned motion paths	Well-established standard approach	Takes considerably more time to survey large areas
Non-uniform survey	Typically controlled by human operator	Increased accuracy/precision in area of interest	Dependent on human operations
Multi-sensor uniform survey	Possible through pre-planned motion paths	Decrease in survey time compared to single-sensor survey	Prone to complexities in motion path planning
Multi-sensor non-uniform survey	Typically controlled by human operator	Improved coverage in area of interest compared to single-sensor survey	Requires multiple human operators

The methods for coverage of an unknown environment using multi-vehicle systems relies on the ability to characterize a density function of a scalar field [12–15]. The optimal solutions to the coverage control problem for unknown density functions have previously been shown; specifically, the use of Gaussian processes to describe unknown density functions of the scalar field is particularly convenient [16–19]. Previous approaches relevant to this work implement Gaussian process regressions in combination with control laws based on centroidal Voronoi tessellations, where the control algorithms are governed by information entropy to reduce prediction uncertainty [17–19].

In this work, we implement Gaussian process regressions (GPR) to predict the unknown density function similar to the approaches in [16–19]. However, rather than using the minimization of information entropy to govern the control laws, we propose to use the difference in successive predicted density functions. The difference in successive maps, hereafter referred to as the prediction-difference map, provides information that points toward the direction of the largest discrepancy between the current and previously predicted scalar fields to produce a convergent map. We show in simulations that the proposed motion planning procedure can offer a fully autonomous controls platform that reduces the overall survey time to reach a convergent radiation contamination map and does not require human-in-the-loop operations. Although the results shown in this work assume velocities more suitable for UAV systems, the fundamental methods can be applied to any available distributed UAV/UGV systems that have autonomous control capabilities as the technique ultimately provides optimal motion trajectories regardless of vehicle type.

The paper is structured as follows: Section 2 describes the radiation transport simulations used to create datasets representing radiological contamination in large areas. Section 3 details the standard GPR model for predictive mapping and the underlying assumptions. In Section 4, we describe how the difference in successive GPR full-map prediction provides prediction-difference maps, which is then used as the spatial density function to inform control laws for centroidal Voronoi tessellations. In Section 5, the simulated dataset of radiation contamination in a one-square kilometer area is used to test and verify the proposed motion planning procedure for a varied number of mobile radiation detectors, and is directly compared to uniform surveying techniques as a function of overall survey time. We draw conclusions and comment on future work in Section 6.

2. Simulations of Radiation Contamination Using MCNP 6.2

Monte Carlo N-particle (MCNP) is a general-purpose Monte-Carlo-based code developed and maintained at Los Alamos National Laboratory, used for particle transport

simulations. The code allows users to establish application-specific geometries and source terms to simulate the expected outcomes from particle transport through various materials; quantities such as radiation dose rates can be calculated. In this work, we simulated radiation contamination by using MCNP6.2 [20] to create datasets for testing the proposed mapping technique. A one-square-kilometer area consisting of several distinct contamination locations with varying levels of activity was simulated. The three main contamination sites consisted of many large circular surface sources emitting mono-energetic gamma rays from the decay of radioactive Cs-137 (i.e., at 662 keV). Each circular source had an assumed surface depth of 1 cm, and the gamma rays were emitted isotropically with varying radii between 65 to 150 m. The spatial emission profile within each surface source is uniform and perfectly flat. The total activity for all three contamination sites were scaled to be roughly twice the background level. The gamma rays are transported through dry sea-level atmospheric air [21], and a Cartesian mesh tally is imposed on the one-square-kilometer area at a predefined survey altitude to assess the flux at any volume element of 5 m $\times$ 5 m $\times$ 5 m. For each volume element, MCNP6.2 calculates an average areal flux in units of γ/cm^2-s, which is used as the effective areal sensitivity of a given detector (i.e., 100% efficiency). A flux-to-dose conversion is implemented through the MCNP6.2 built-in dose-conversion functions that utilize the ICRP 60 standards [20]. The ground-level material is soil with a depth of 30 cm; with an elemental composition of hydrogen (weight fraction of 2.4%), oxygen (weight fraction of 59.8%), aluminum (weight fraction of 8.0%), and silicon (weight fraction of 29.7%) [21]. Assuming an average activity of 0.59 Bq/g from the soil [22] and a soil density of 1.52 g/cm^3 [21], the total activity solely from the soil is approximately 2.7×10^{11} Bq. Background radiation from the soil was simulated as random fluctuations by taking samples from a Gaussian distribution with a mean equivalent to the average activity per volume of approximately 0.90 Bq/cm^3 at ground level. We assume a survey altitude of 40 m in this work to demonstrate a typical flight altitude of rotor-copter-type UAVs. Figure 1 shows the simulated dose rate distribution within the area of interest at an altitude of 40 m.
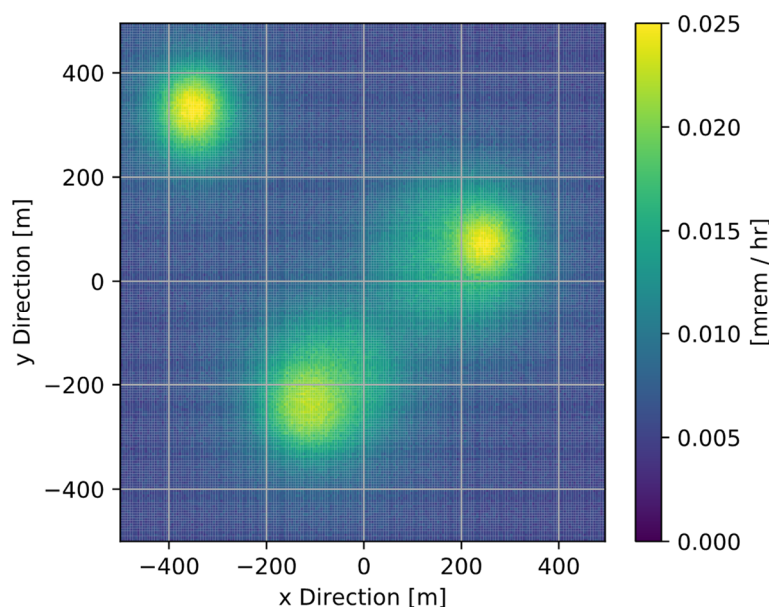

Figure 1. Simulated radiation contamination site showing gamma-ray dose rate distribution. Global average of terrestrial background dose rate is approximately 5.5×10^{-3} mrem/h.

3. Gaussian Process Regression Model for Radiation Contamination Mapping

GPR is a non-parametric regression technique, where the data is modeled as a Gaussian process (*GP*). A *GP* is defined as a collection of random variables where any finite number of the random variables have a joint Gaussian distribution [23,24]. The output of a *GP*

model, $y = f(x)$ is fully described in terms of the input, x, with the mean function $m(x)$ and the covariance function $k(x, x')$ defined as:

$$m(x) = \mathbb{E}[f(x)], \tag{1}$$

$$k(x, x') = \mathbb{E}[f(x) - m(x))(f(x') - m(x'))]. \tag{2}$$

The *GP* can empirically be written as:

$$y = f(x) \sim GP(m(x), k(x, x')). \tag{3}$$

To apply the GPR technique for predicting dose rates from the detected count rates, and in turn, the contamination at various locations in the area of interest, we define the collection of previously observed data as $(P = (p_1, ..., p_n^\top), c = (c_1, ..., c_n)^\top)$ where c is an $n \times 1$ vector containing the radiation count rate, and P is an $n \times 2$ matrix that contains two features describing the location (i.e., the corresponding latitudinal and longitudinal coordinates) for n observations [24]. This model assumes that the observed count rate c behaves as a normal distribution about the corresponding mean count rate $m(p)$ for observation location p, with a covariance directly related to the relationship between all observation locations (e.g., p and $(p_1, \ldots, p_n)$). Using the aforementioned definitions and employing the properties of *GP*, we define the GPR model as

$$\begin{pmatrix} c_* \\ c_1 \\ \vdots \\ c_n \end{pmatrix} \sim \mathcal{N}\left(\mu = \begin{pmatrix} m(p_*) \\ m(p_1) \\ \vdots \\ m(p_n) \end{pmatrix}, \Sigma = \begin{pmatrix} k_{**} & k_{*.} \\ k_{.*} & k_{..} \end{pmatrix} \right), \tag{4}$$

with the components of the covariance matrix Σ defined as

$$k_{**} = k(p_*, p_*), \tag{5}$$

$$k_{*.} = (k(p_*, p_1), \cdots, k(p_*, p_n)), \tag{6}$$

$$k_{.*} = (k(p_1, p_*), \cdots, k(p_n, p_*))^\top, \tag{7}$$

$$k_{..} = \begin{pmatrix} k(p_1, p_1) & \cdots & k(p_1, p_n) \\ \vdots & \ddots & \vdots \\ k(p_n, p_1) & \cdots & k(p_n, p_n) \end{pmatrix}. \tag{8}$$

In (4), we use the collection of observed data $c_1, \ldots, c_n$ and the corresponding features $p_1, \ldots, p_n$ to train the model, and subsequently predict the unknown count rates c_* that correspond to unvisited locations P_*; c_* is a $u \times 1$ vector containing the predicted count rates at P_*, which is a $u \times 2$ matrix containing the latitudinal and longitudinal coordinates of the unvisited locations for the u remaining locations. The components of the covariance matrix in (5)–(8) implicitly characterize the similarity between the mean count rates based on the Euclidean distance between any and all observation locations. For example, the similarity between mean count rates $m(p_1)$ and $m(p_2)$ is described by some covariance function $R(|p_1 - p_2|)$ In typical applications of GPR, the covariance function has the form of

$$k(p_i, p_j) = \sigma^2 R\left(\left|p_i - p_j\right|\right) = \sigma^2 R(r), \tag{9}$$

where r is the Euclidean distance between the two inputs p_i and p_j, σ^2 is the variance of the *GP*, and $R(r)$ is the correlation kernel function used to describe the shape of the covariance relative to the Euclidean distance r and allows for mapping of a pair of inputs—here the observation locations—into an n-dimensional domain R^n [23,24]. The variance of the *GP* can be included along with the covariance to estimate a combined uncertainty that

considers uncertainties independent of the predictions made. There are many commonly used kernels for describing the covariance function and several different types were tested in this work by using a five-fold cross-validation test [23]. The cross-validation testing involves taking a fixed number of random samples from the data to be used as the training set, whereas the remaining partition of the data is used as the test set to evaluate the fidelity of the kernel used detailed in Section 3.2. Using the GPR model described in (4), the observed count rates and the respective latitudinal and longitudinal coordinates are used as input data and the remaining unvisited locations P_* are used to predict the respective count rates c_*. Once all the count rates at the unvisited locations are predicted, it can be projected as a two-dimensional grid corresponding to their respective locations. The predicted GPR full-map is defined as

$$\phi(g), \quad for \ g \in G, \quad G \subset \mathbb{R}^2. \tag{10}$$

3.1. GPR Implementation in Python

The GPR predictions were done by using the Python Scikit-learn (sklearn) library, which has many built-in functions used for standard regression techniques [25]. Specifically, the sklearn.preprocessing and sklearn.gaussian_regression modules are used in this work. The StandardScaler option within sklearn.preprocessing is used to standardize the features by centering the mean to zero and scaling to unit variance. This allows for a more consistent behavior in the regression due to many of the kernel covariance functions requiring the data to represent a standard normal distribution, such as a Gaussian, with zero mean and unit variance [23,25]. GPR is performed on the scaled dataset by using the sklearn.gaussian_regression module, and subsequently transformed back to its original scale. The sklearn.gaussian_regression module also contains all the standard kernel covariance functions tested in this work, which include the radial basis function, rational quadratic function, and the Matérn function. The GPR analysis gives the output and corresponding standard deviations for each prediction, providing some quantity to assess the confidence in the prediction. A maximum likelihood estimation method for the parameters in the GPR model and kernel correlation function is used at each predicted iteration, and solved by using the built-in limited-memory Broyden–Fletcher–Goldfarb–Shanno (L-BFGS) optimizing algorithm [26]. We conducted a case study using a k-fold cross-validation test to (a) demonstrate the validity of using a GPR model for radiation contamination mapping and (b) investigate the optimal kernel for the covariance function that best describes the simulated data, and in turn the underlying physics for gamma-ray transport in air.

3.2. K-Fold Cross-Validation Test

We use the sklearn.model selection module to perform a five-fold cross validation test on a dataset comprised of 5000 total data points for a number of different standard kernels to describe the covariance function [23,25]. The simulated data was structured as defined by (4), where Y contained the flux-converted dose rates at locations described by X. For a given jth fold of the cross-validation test, the data from $j \times 1000$ to $(j + 1) \times 1000$ are used to train the GPR model, and the remaining 4000 data points are subsequently used as the test data. For each j-fold test case, the mean relative difference between the true and the predicted values from the test data are calculated; the results from all iterations of the five-fold cross validation test are shown in Table 2 for each tested covariance function. The $\alpha > 0$ and $l \geq 1$ are the scale mixture and length-scale parameters, respectively, and were free parameters for the five-fold cross validation tests [25]. In principle, a similar k-fold cross validation test can be performed to investigate the optimal kernel covariance function if the data is expected to behave differently than gamma-ray transport through air and if prior datasets are available.

The results in Table 1 show that the Matérn kernel ($\nu = \frac{1}{2}$) gives the lowest average relative deviation, and was chosen to be the most suitable kernel for the covariance function.

Table 2. Five-fold cross-validation results for all tested covariance functions.

Kernel	Radial Basis Function	Rational Quadratic	Matérn ($v = \frac{1}{2}$)	Matérn ($v = \frac{3}{2}$)	Matérn ($v = \frac{5}{2}$)
Functional Form R(r)	$\exp\left(-\frac{r^2}{2l^2}\right)$	$\exp\left(1+\frac{r^2}{2\alpha l^2}\right)^a$	$\exp\left(-\frac{1}{l}\cdot r\right)$	$\left(1+\frac{\sqrt{3}}{l}\cdot r\right)\cdot$ $\exp\left(-\frac{\sqrt{3}}{l}\cdot r\right)$	$\left(1+\frac{\sqrt{5}}{l}\cdot r+\frac{5}{3l}\cdot r^2\right)\cdot$ $\exp\left(-\frac{5}{l}\cdot r\right)$
Fold 1	0.118	0.057	0.052	0.060	0.069
Fold 2	0.133	0.057	0.051	0.061	0.071
Fold 3	0.131	0.053	0.048	0.060	0.070
Fold 4	0.121	0.056	0.051	0.062	0.072
Fold 5	0.141	0.055	0.052	0.062	0.074
Average	**0.129**	**0.056**	**0.051**	**0.061**	**0.071**

4. Optimal Motion Planning Using Voronoi Partitions and Prediction Difference Maps

The GPR predicted full-map provides the basis for the optimal motion planning procedures at every instance a prediction is made. We adopt the method originally described by Martinez et. al. that utilizes Voronoi diagrams as a means to achieve ideal coverage for distributed networked mobile sensors [12–14]. Some of the key advantages of using Voronoi partitions to establish optimal motion planning include (a) the method inherently includes UAV-sensor collision avoidance, which can be a complicated problem to solve [27], and (b) the method is scalable to any number of UAV-sensors [12–14]. Given discrete grid locations g within a predefined area $G \subset R^2$, and a set $S = \{s_1,..., s_N\} \subset G$ of N sensors in distinct locations where s_n contains the x and y coordinates, we define the Voronoi partitions generated by S as the collection of sets $V = V_1(S), \ldots V_N(S)$ where $V_i(S)$ is defined as:

$$V_n(S) = \{g \in G \mid \|g - s_n\| \leq \|g - s_m\|, \quad for\ all\ s_m \in S\} \tag{11}$$

and refer to (11) as the Voronoi cell of sensor s_n [12–14,16–19]. Equation (11) states that the Voronoi cell V_n consists of all the points within the entire area of interest whose distance to sensor s_n is less than or equal to its distance to any other sensor s_m. Suppose we have a recursive framework where j represents each instance of observations from n sensors. For every iteration j, the GPR model predicts the full-map $\phi_j(g)$ and the prediction-difference map (PDM), defined as the absolute difference between the current and prior GPR predicted full-map is calculated by using

$$\Psi(g) = \left|\phi_j(g) - \phi_{j-1}(g)\right|. \tag{12}$$

The PDM is used as the density function describing the difference in prior and current predicted features throughout the entire area. The full PDM is partitioned for each Voronoi cell (i.e., each sensor region), Ψ_n, which describes a density function outlining the largest discrepancies between successive observations. Using the concepts of centroidal Voronoi tessellations, it was demonstrated in [13] that the local minimum points for optimizing the objective function in each Voronoi cell are simply the density-function-weighted centroids. Therefore, we establish a navigation policy that is based on moving toward the direction of the center of mass by using the PDM as the spatial density function to describe the contamination in each Voronoi cell. The mass and the center of mass for PDM-weighted Voronoi cell are calculated by using

$$M_{V_{n,\,j}} = \sum_{V_{n,j}} \Psi_n \tag{13}$$

and

$$CM_{V_{n,j}} = \frac{1}{M_{V_{n,j}}} \sum_{V_{n,j}} g\Psi_n, \ \ for \ g \ \in V_{n,j}. \tag{14}$$

Assuming that the sensors can move in any direction relative to its current location $s_{n,j}$, we set the x and y direction of the sensor's trajectory as

$$\widehat{x_n} = \frac{\left(CM_{V_{n,j}} - s_{n,j} \right)_x}{\left| \left(CM_{V_{n,j}} - s_{n,j} \right)_x \right|} \tag{15}$$

and

$$\widehat{y_n} = \frac{\left(CM_{V_{n,j}} - s_{n,j} \right)_y}{\left| \left(CM_{V_{n,j}} - s_{n,j} \right)_y \right|} \ , \tag{16}$$

which directs the sensors towards the centroid of each respective PDM-weighted Voronoi cell Ψ_n. Subsequently, the change in sensor position is calculated by using

$$\boldsymbol{u_n} = v \cdot (\widehat{x_n} + \widehat{y_n}), \tag{17}$$

where v is the velocity of the UAV.

Figure 2 shows an example of the spatial density function weighted Voronoi cells produced by a five-sensor survey.

We developed a simulation framework for modeling survey routes by using multiple UAVs in Python to demonstrate the PDM-based motion planning procedure. The model takes as input the number of UAV sensors, velocity, dwell time per measurement location, and initial starting positions, which are then used to simulate the movement of the UAVs by using the direction given by the optimal motion planning procedure. Algorithm 1 provides the details for the recursive framework for the PDM-based motion planning procedure.

Algorithm 1. Recursive Motion Planning

---

1.   **Initialize:** $s_1, \ldots, s_n; \ \phi_{j=0}(g) = 0; l_{j=0} = 1$
2.   **Predict:** $\phi_j(g)$ with $P_{j=0} \leftarrow s_1, \ldots, s_n;$
3. $c_{j=0} \leftarrow c_{s_1}, \ldots, c_{s_n}; \ \boldsymbol{P^*}; \boldsymbol{c^*}; l_{j=0}$
4.   **Optimize:** l_j
5.   **While $\boldsymbol{\phi_j(g)}$ not converged**:
6.   **Calculate:** $\Psi(g) \leftarrow \left| \phi_j(g) - \phi_{j-1}(g) \right|$
7.   **For n in N sensors do**
8.   **Compute:**
9. $V_{n,\,j}(S) \leftarrow \left\{ g \in G \middle| \ \|g - s_{n,\,j}\| \leq \|g - s_{m,\,j}\| \ , for \ all \ s_{m,\,j} \in S \right\}$
10. $M_{V_{n,j}} \leftarrow \sum_{V_{n,j}} \Psi_n$
11. $CM_{V_{n,j}} \leftarrow \frac{1}{M_{V_{n,j}}} \sum_{V_{n,j}} g \cdot \Psi_n$
12. $\widehat{x_n} \leftarrow \frac{(CM_{V_n} - s_n)_x}{|(CM_{V_n} - s_n)_x|}; \ \widehat{y_n} \leftarrow \frac{(CM_{V_n} - s_n)_y}{\left|(CM_{V_n} - s_n)_y\right|};$
13. $\boldsymbol{u_n} \leftarrow v \cdot (\widehat{x_n} + \widehat{y_n})$
14. $s_n \leftarrow \left[(s_n)_x + (u_n)_x, \ (s_n)_y + (u_n)_y \right]$
15.   **For $t \leq T_{dwell}$:**
         $c(s_n) \leftarrow c(s_n) + c(s_n, \ t)$
         $c_{s_n} = \frac{c(s_n)}{T}$
16.   **Append:** $P, \ \boldsymbol{s_n}; c, c_{s_n}$
17. $\phi_{j-1} \leftarrow \phi_j; l_{j-1} = l_j$
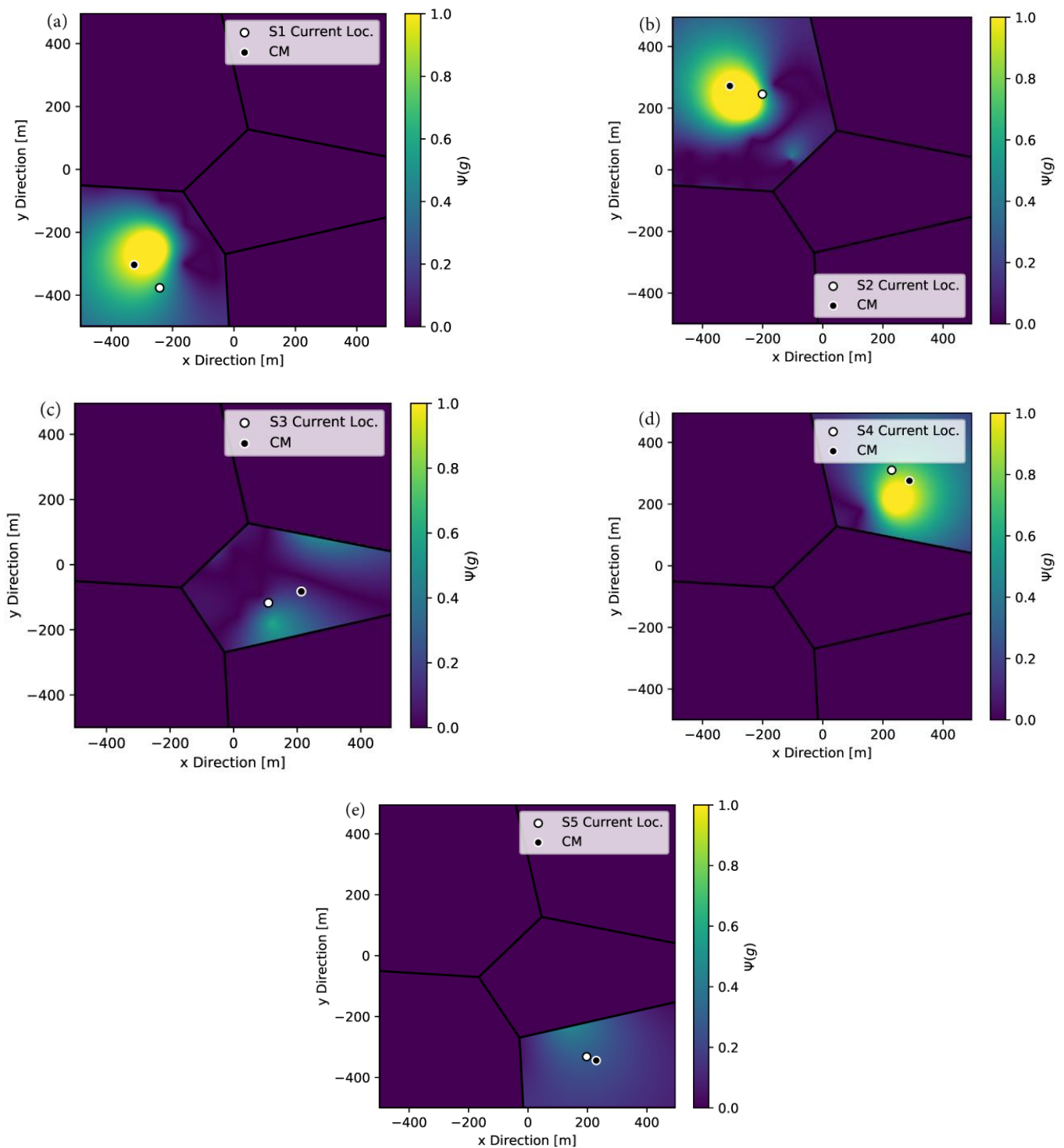18.   **Predict:** $\phi_j(g)$ with $P; \boldsymbol{c} \ ; P^* \leftarrow p_u; c^* \leftarrow c_{p_u}; l_j$

Figure 2. The PDM weighted Voronoi cells for a five-sensor survey showing the current sensor location and the calculated center of mass for (**a**) sensor 1, (**b**) sensor 2, (**c**) sensor 3, (**d**) sensor 4, and (**e**) sensor 5. The color bar represents the absolute fractional difference between successive predicted maps.

Operational implementation of the proposed PDM-based motion planning procedure would involve establishing UAV/UGV-specific control parameters such as velocity, flight altitude for UAVs, and dwell times that will enable statistically confident count rates for the radiation detector of choice. The dwell times could be dynamically set for each observation location based on the real-time sensor data.

5. Results and Discussion

To quantify the grid-by-gird accuracy of the predicted map, we compare each of the estimated grid locations in the entire area of interest to the true simulated distribution using

$$E = 1 - \frac{\sum_{g \in G} \left| \phi_{true}(g) - \phi_{pred}(g) \right|}{\sum_{g \in G} \phi_{true}(g)} \; , \tag{18}$$

where $\phi_{true}(g)$ is the simulated flux distribution provided by MCNP6.2, and $\phi_{pred}(g)$ is the convergent predicted contamination map given by the GPR model. The results for the five- and seven-sensor survey using the PDM-based motion planning procedure are presented in Figures 3 and 4; the true distribution is shown in Figure 1. The velocity was set to 5 m/s with a dwell time of 5 s per measurement location, where we assume a rotocopter type UAV for this study [2], but the presented algorithm is applicable to any type of UAV or UGV that is able to turn in any direction from its current position. The initial starting positions of the UAV sensors were distributed in the southern region of the one-square-kilometer predefined survey area to demonstrate a case where the UAV sensors are deployed from a common destination. The predicted contamination map in Figures 3 and 4 are for an *E* value of 0.90 (i.e., 90% mean accuracy), the choice of 0.90 is used here for visual purposes.
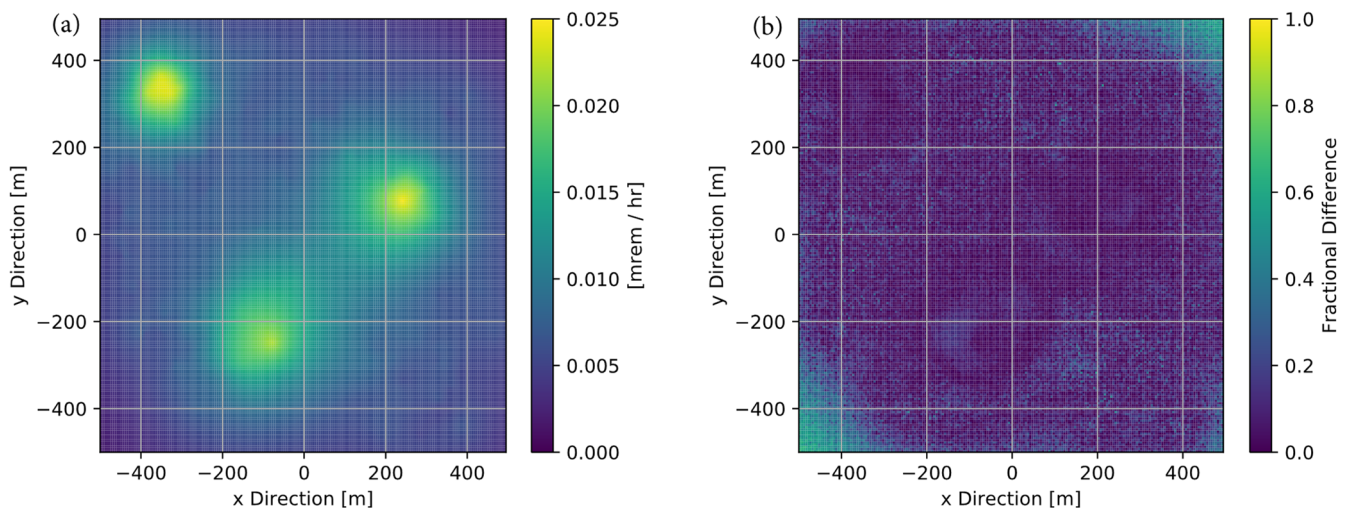

Figure 3. Five-sensor survey results showing (**a**) the predicted distribution for *E* = 0.90 and (**b**) the grid-by-grid fractional difference to the true distribution shown in Figure 1.

Figure 5 shows the optimized motion-path trajectories from the PDM-based mapping routine overlaid on the predicted distributions.

The GPR-predicted full-maps also provide prediction uncertainties for unvisited locations within the area of interest, which is a unique feature unavailable to the traditional uniform survey methods that can only provide statistical uncertainties and in turn confidence intervals at the visited locations. Figure 6 shows the GPR predicted values for dose rates through y = 0, where the true distribution is primarily contained within the 95% confidence interval of the predicted values. It is important to note here that there is no prediction uncertainty in the observed locations because no prediction is made but rather an actual observation. Therefore, the uncertainty in the visited locations would in principle reflect the counting statistics obtained based on the type of detector used, source strength, and the dwell time. As the number of visited locations increases (i.e., longer survey times), the prediction uncertainty of the overall full-map prediction would decrease as there would be fewer unvisited locations and in turn fewer predictions made.
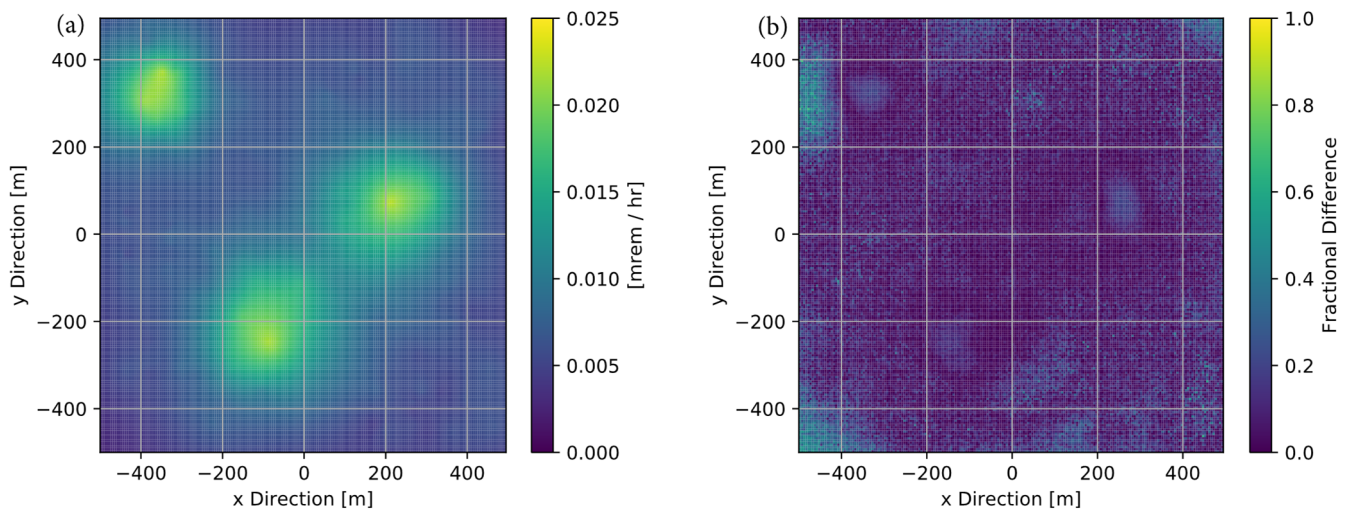
Figure 4. Seven-sensor survey results showing (**a**) the predicted distribution for $E = 0.90$ and (**b**) the grid-by-grid fractional difference to the true distribution shown in Figure 1.
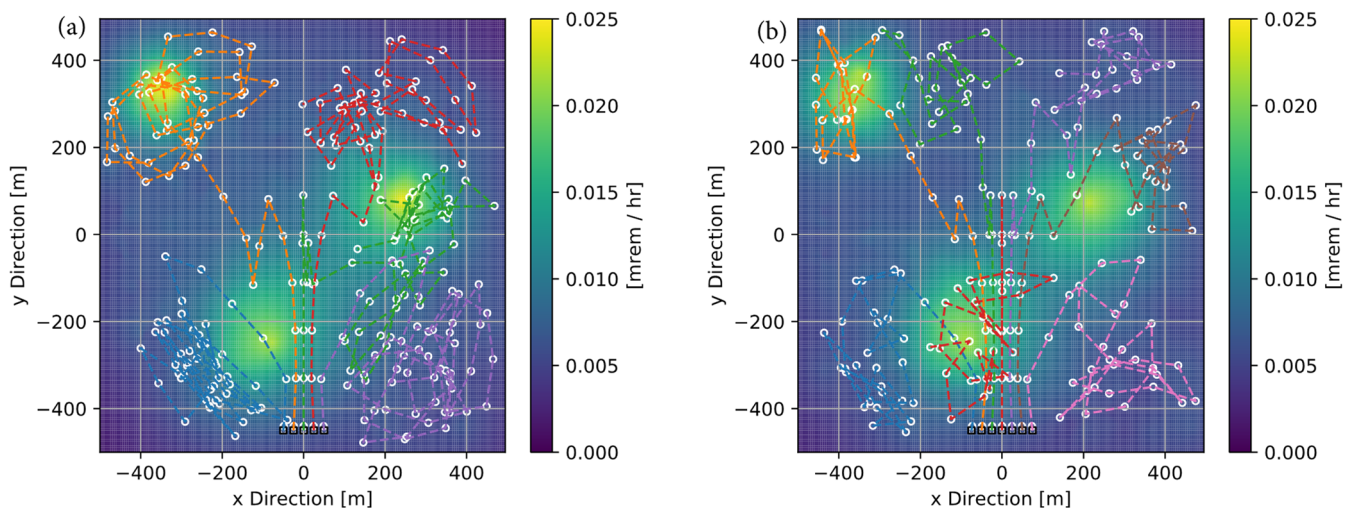

Figure 5. Optimized motion path trajectories dictated by the PDM-informed motion planning procedure for (**a**) the five-sensor and (**b**) seven-sensor surveys. The white markers represent locations where a measurement has been taken.

An important distinction from typical uniform survey routines, the prediction uncertainty provided by the GPR maps is independent of knowing the true magnitude of the radiation contamination at a location but rather reflects the uncertainty based on the vicinity of the unvisited locations to the visited locations. In practice, the prediction uncertainty can be used to establish a quantitative metric for deciding a stopping criterion for the mapping routine in addition to the statistical uncertainties at visited locations that arise from the instruments used as well as the established dwell time. For example, the amount of additional survey time required to reach a desired accuracy could be inferred from the prediction uncertainties.
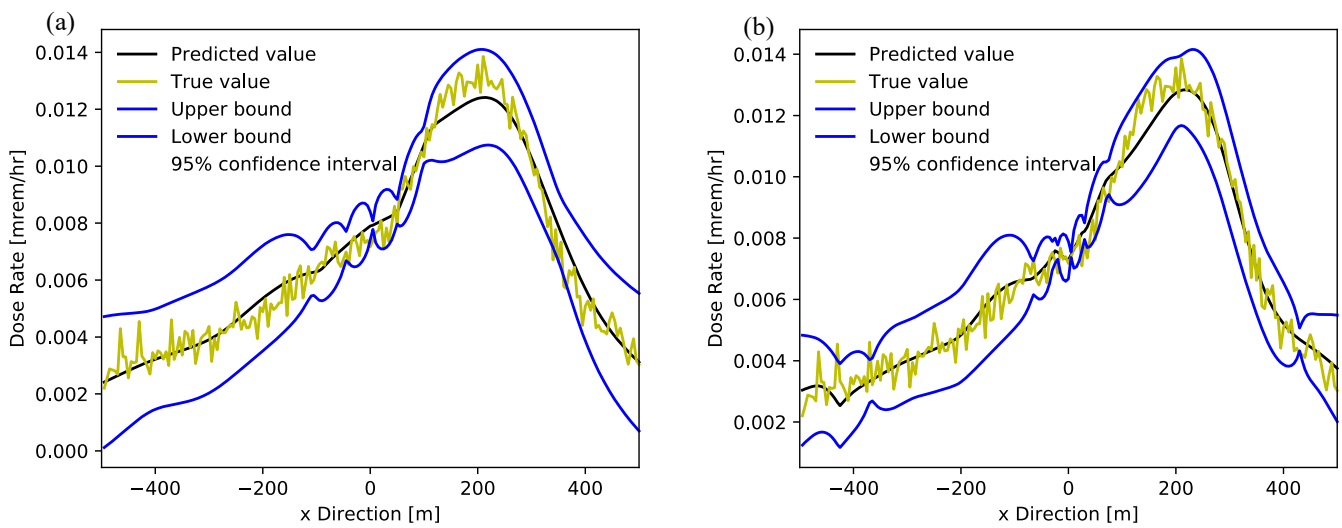
Figure 6. The calculated prediction uncertainty through y = 0 for (**a**) the five-sensor and (**b**) seven-sensor surveys demonstrating that prediction uncertainties decrease near the vicinity of observed locations.

To confirm that the PDM-based mapping routine converges to a result similar to that achieved by a typical uniform survey routine, we approximated a raster-type survey by uniformly sampling the survey area where each measurement location is separated by 25 m and 50 m, resulting in a grid-by-grid accuracy of 0.93 and 0.88 using (18), respectively. Figures 7 and 8 shows the uniformly sampled survey area along with the fractional difference to the true distribution. The separation between measurement locations were chosen to reflect a final accuracy comparable to the PDM-based mapping routine. The accuracy and survey time of the uniform surveys will change based on the separation of measurement locations; larger separations produce a less-accurate but faster survey while smaller separations produce a more accurate but slower survey.
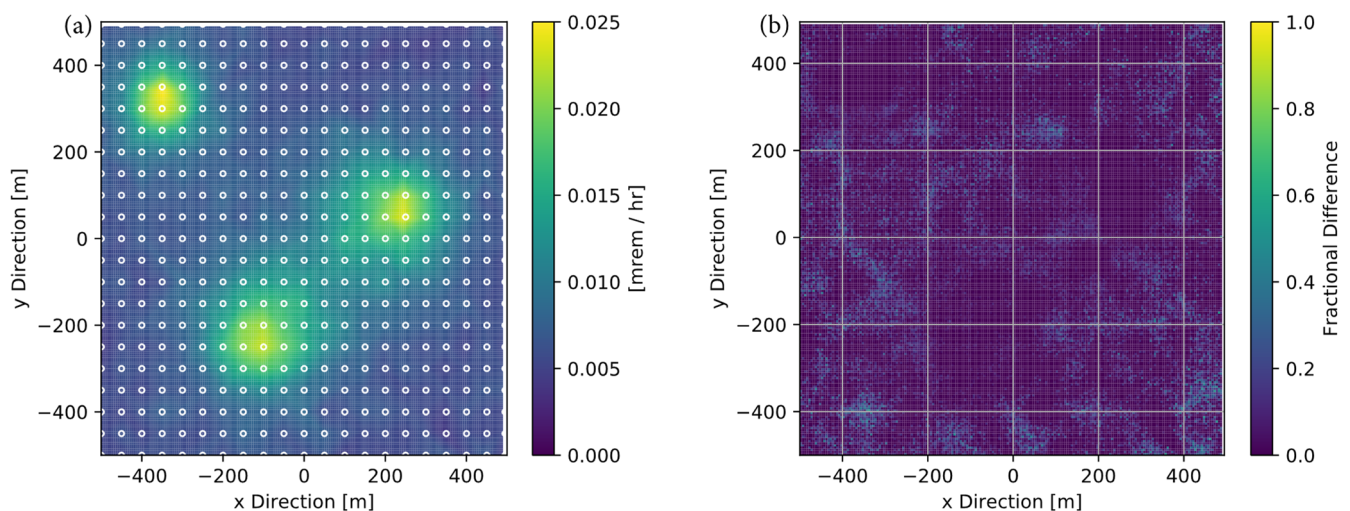

Figure 7. (**a**) Uniform measurement locations with measurements taken every 50 m and linearly interpolated between observation points, and (**b**) the grid-by-grid fractional difference to the true distribution shown in Figure 1. The white markers represent locations where a measurement has been taken.
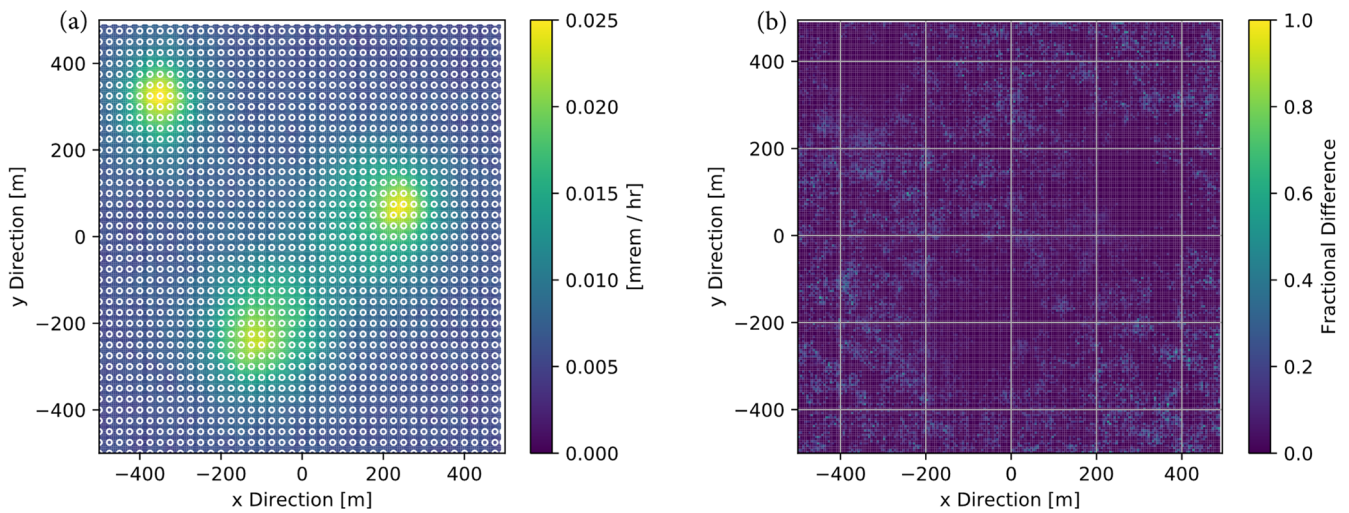
Figure 8. (**a**) Uniform measurement locations with measurements taken every 25 m and linearly interpolated between observation points, and (**b**) the grid-by-grid fractional difference to the true distribution shown in Figure 1. The white markers represent locations where a measurement has been taken.

The dose rate distributions shown in Figures 7 and 8 are given by implementing a two-dimensional linear interpolation between all sampled measurement locations. A raster-type motion path (from left to right and from top to bottom) for the uniform survey routine was simulated by using five and seven sensors with the same speed and dwell time as the PDM-based mapping routine. Figure 9 shows a comparison of E as calculated by (18) for GPR-predicted maps from the PDM-based routine versus the uniform survey routine. Figure 9 demonstrates that the PDM-based mapping routine provides a convergent map at a faster rate than using uniform survey routines, and that it does indeed converge to the expected results from a uniform survey routine.
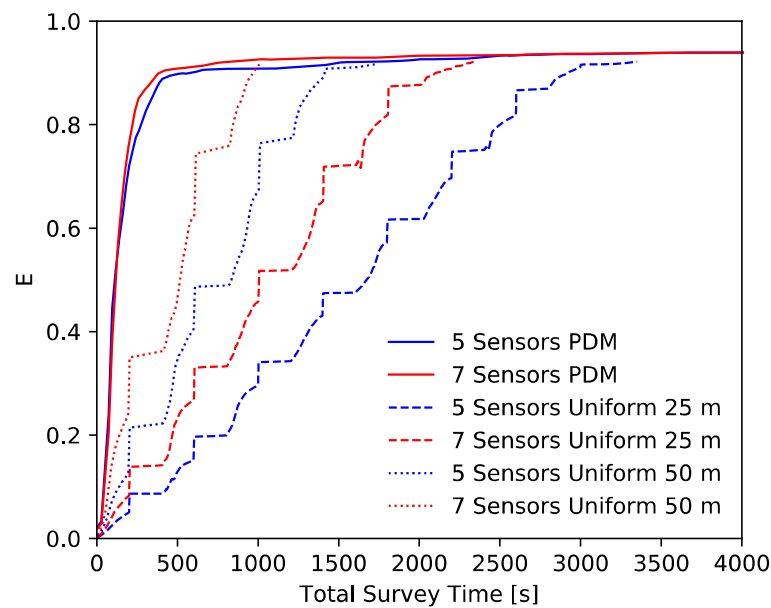

Figure 9. Direct comparison of the PDM-based survey routine results versus the uniform survey results as a function of the total survey time. The uncertainty in E for the GPR-predicted maps is represented by the prediction uncertainties shown in Figure 8.

Furthermore, the ability for the PDM-based routine to provide actionable information at an appreciably faster rate is demonstrated due to its capability for predicting locations

that have not yet been visited. In practice, the information in Figure 9 would not be available as the true magnitude of the contamination is unknown; however, the figure demonstrates that our PDM-based motion planning procedure allows the sensors to move more efficiently than for uniform scanning, while arriving at the same result.

6. Conclusions

We have developed a prediction-difference-map (PDM)-based optimal motion planning routine by using Gaussian process regression and well-established control laws for centroidal Voronoi tessellations. By using the PDMs as the density function in our motion planning procedure, we demonstrate that a continuously informed method for optimizing UAV sensor movements is possible. The approach and results outlined in this work demonstrate that PDM-based survey routines can provide actionable information more quickly than traditional uniform survey routines. We also showed that our method provides an estimate of the prediction uncertainty of the unvisited locations, which can be used to establish a quantitative convergence criterion that augments qualitative inspection of the predicted map.

Using the PDM-based motion planning procedure can improve on the speed of producing contamination maps to provide actionable information in time-sensitive scenarios. Furthermore, because battery life is a major operational limitation for UAV-sensors, PDM-based motion planning can provide a more informative understanding of contamination in a large area for fixed flight times. Another advantage of the PDM-based motion planning procedure is that it does not assume any prior distribution of the contamination but rather dynamically uses the sensor data to produce optimal motion trajectories. Without any assumptions on the prior distribution of the contamination, there should be no dependency on the number of sensors, sensor starting positions, number of contamination sites, the shape/size of the contamination, and the overall scale of the search area; the proposed algorithm will still produce convergent results. PDM-based optimal motion planning is a robust and situation-agnostic approach that can be implemented for any arrangement of number and types of mobile and static sensors.

Author Contributions: Conceptualization, T.H.S.; Data curation, T.H.S.; Formal analysis, T.H.S.; Funding acquisition, T.H.S., D.T.W. and S.F.N.; Investigation, T.H.S.; Methodology, T.H.S., D.T.W. and S.F.N.; Writing—original draft, T.H.S.; Writing—review & editing, D.T.W. and S.F.N. All authors have read and agreed to the published version of the manuscript.

Conflicts of Interest: The authors declare no conflict of interest.

References

1. Martin, P.G.; Payton, O.D.; Fardoulis, J.S.; Richards, D.A.; Scott, T.B. The use of unmanned aerial systems for the mapping of legacy uranium mines. *J. Environ. Radioact.* **2015**, *143*, 135–140. [CrossRef] [PubMed]
2. Connor, D.; Martin, P.G.; Scott, T.B. Airborne radiation mapping: Overview and application of current and future aerial systems. *Int. J. Remote Sens.* **2016**, *37*, 5953–5987. [CrossRef]
3. Sanada, Y.; Torii, T. Aerial radiation monitoring around the Fukushima Dai-ichi nuclear power plant using an unmanned helicopter. *J. Environ. Radioact.* **2015**, *139*, 294–299. [CrossRef] [PubMed]
4. Jiang, J.; Shimazoe, K.; Nakamura, Y.; Takahashi, H.; Shikaze, Y.; Nishizawa, Y.; Yoshida, M.; Sanada, Y.; Torii, T.; Yoshino, M.; et al. A prototype of aerial radiation monitoring system using an unmanned helicopter mounting a GAGG scintillator Compton camera. *J. Nucl. Sci. Technol.* **2016**, *53*, 1067–1075. [CrossRef]
5. Pollanen, R.; Toivonen, H.; Perajarvi, K.; Karhunen, T.; Ilander, T.; Lehtinen, J.; Rintala, K.; Katajainen, T.; Niemala, J.; Juusela, M. Radiation Surveillance using an unmanned aerial vehicle. *Appl. Radiat. Isot.* **2009**, *67*, 340–344. [CrossRef] [PubMed]
6. Martin, P.; Kwong, S.; Smith, N.; Yamashiki, Y.; Payton, O.; Russell-Pavier, F.; Fardoulis, J.; Richards, D.; Scott, T. 3D unmanned aerial vehicle radiation mapping for assessing contaminant distribution and mobility. *Int. J. Appl. Earth Obs. Geoinf. ITC J.* **2016**, *52*, 12–19. [CrossRef]
7. Towler, J.; Krawiec, B.; Kochersberger, K. Terrain and Radiation Mapping in Post-Disaster Environments Using an Autono-mous Helicopter. *Remote Sens.* **2012**, *4*, 1995–2015. [CrossRef]

8. Han, J.; Chen, Y. Multiple UAV Formations for Cooperative Source Seeking and Contour mapping of a Radiative Signal Field. *J. Intell. Robot. Syst.* **2014**, *74*, 323–332. [CrossRef]

9. Han, J.; Xu, Y.; Di, L.; Chen, Y. Low-cost Multi-UAV Technologies for Contour Mapping of Nuclear Radiation Field. *J. Intell. Robot. Syst.* **2012**, *70*, 401–410. [CrossRef]

10. Kurvinen, K.; Smolander, P.; Pöllänen, R.; Kuukankorpi, S.; Kettunen, M.; Lyytinen, J. Design of a radiation surveillance unit for an unmanned aerial vehicle. *J. Environ. Radioact.* **2005**, *81*, 1–10. [CrossRef] [PubMed]

11. Boudergui, K.; Carrel, F.; Domenech, T.; Guenard, N.; Poli, J.P.; Ravet, A.; Schoepff, V.; Woo, R. Development of a Drone Equipped with Optimized Sensors for Nuclear and Radiological Risk Characterization. In Proceedings of the 2nd International Conference on Advancements in Nuclear Instrumentation, Measurement Methods and their Applications, Ghent, Belgium, 6–9 June 2011.

12. Martinez, S.; Cortes, J.; Bullo, F. Obtaining Global Behavior from Local Interaction. *IEEE Control Syst.* **2007**, *27*, 75–88.

13. Cortes, J.; Martinez, S.; Karatas, T.; Bullo, F. Coverage Control for Mobile Sensing Networks. *IEEE Trans-Actions Robot. Autom.* **2004**, *20*, 243–255. [CrossRef]

14. Cortés, J.; Martínez, S.; Bullo, F. Spatially-distributed coverage optimization and control with limited-range interactions. *ESAIM: Control. Optim. Calc. Var.* **2005**, *11*, 691–719. [CrossRef]

15. Du, Q.; Faber, V.; Gunzburger, M. Centroidal Voronoi Tessellations: Applications and Algorithms. *SIAM Rev.* **1999**, *41*, 637–676. [CrossRef]

16. Gu, D.; Hu, H. Spatial Gaussian Process Regression with Mobile Sensor Networks. *IEEE Trans. Neural Netw. Learn. Syst.* **2012**, *23*, 1279–1290. [CrossRef] [PubMed]

17. Carron, A.; Todescato, M.; Carli, R.; Schenato, L.; Pillonetto, G. Multi-agents adaptive estimation and coverage control using Gaussian regression. In Proceedings of the 2015 European Control Conference (ECC), Linz, Austria, 15–17 July 2015; pp. 2490–2495. [CrossRef]

18. Luo, W.; Sycara, K. Adaptive Sampling and Online Learning in Multi-Robot Sensor Coverage with Mixture of Gaussian Processes. In Proceedings of the 2018 IEEE International Conference on Robotics and Automation (ICRA), Brisbane, QLD, Australia, 21–25 May 2018; pp. 6359–6364. [CrossRef]

19. Luo, W.; Nam, C.; Kantor, G.; Sycara, K. Distributed environmental modeling and adaptive sample for multi-robot sensor coverage. In Proceedings of the 18th International Conference on Autonomous Agents and Multiagent Systems, Montreal, QC, Canada, 13–17 May 2019; pp. 1488–1496.

20. Werner, C.J.; Bull, J.S.; Solomon, C.J.; Brown, F.B.; McKinney, G.W.; Rising, M.E.; Dixon, D.A.; Martz, R.L.; Hughes, H.G.; Cox, L.J.; et al. *MCNP6. 2 Release Notes*; Report LA-UR-18–20808; Los Alamos National Laboratory: Los Alamos, NM, USA, 2018.

21. McConn, R.J., Jr.; Gesh, C.J.; Pagh, R.T.; Rucker, R.A.; Williams, G.R., III. *Compendium of Material Composition Data for Radiation Transport Modeling*; PIET-43741-TM-963, PNNL-15870 Rev. 1; Pacific Northwest National Lab. (PNNL): Richland, WA, USA, 2011.

22. Almlie, J.C. *NORM Primer Industry Edition*; University of North Dakota Energy & Environment Research Center: Grand Forks, ND, USA, 2014. Available online: https://undeerc.org/bakken/optimization/Articles/NORM_Primer_Industry_Edition.pdf (accessed on 1 March 2020).

23. Rasmussen, C.E.; Williams, C.K.I. *Gaussian Processes for Machine Learning*; MIT Press: Cambridge, MA, USA, 2008; ISBN 026218253X. [CrossRef]

24. Liu, Z. Reconstruction of Urban Radiation Landscape using Machine Learning Methods. Ph.D. Dissertation, University of Illinois at Urbana-Champaign, Champaign, IL, USA, 2019.

25. Pedregosa, F.; Varoquaux, G.; Gramfort, A.; Michel, V.; Thirion, B.; Grisel, O.; del, M.B.; Prettenhofer, P.; Weiss, R.; Dubourg, V.; et al. Scikit-learn: Machine learning in Python. *J. Mach. Learn. Res.* **2011**, *12*, 2825–2830.

26. Morales, J.L.; Nocedal, J. Remark on algorithm 778: L-BFGS-B: Fortran subroutines for large-scale bound constrained optimization. *ACM Trans. Math. Softw.* **2011**, *38*, 1–4. [CrossRef]

27. Hussein, I.I.; Stipanovic, D.M. Effective Coverage Control for Mobile Sensor Networks with Guaranteed Collision Avoidance. *IEEE Trans. Control Syst. Technol.* **2007**, *15*, 642–657. [CrossRef]